

Article

Surface Reduction of Li_2CO_3 on LLZTO Solid-State Electrolyte via Scalable Open-Air Plasma Treatment

Mohammed Sahal ¹, Jinzhao Guo ², Candace K. Chan ^{2,*} and Nicholas Rolston ^{1,*}

¹ Renewable Energy Materials and Devices Lab, School of Electrical, Computer and Energy Engineering (ECEE), Arizona State University, Tempe, AZ 85284, USA; mfnu4@asu.edu

² Materials Science and Engineering, School for Engineering of Matter, Transport and Energy (SEMTE), Arizona State University, Tempe, AZ 85287, USA; jguo102@asu.edu

* Correspondence: candace.chan@asu.edu (C.K.C.); nicholas.rolston@asu.edu (N.R.)

Abstract: We report on the use of an atmospheric pressure, open-air plasma treatment to remove Li_2CO_3 species from the surface of garnet-type tantalum-doped lithium lanthanum zirconium oxide ($\text{Li}_{6.4}\text{La}_3\text{Zr}_{1.4}\text{Ta}_{0.6}\text{O}_{12}$, LLZTO) solid-state electrolyte pellets. The Li_2CO_3 layer, which we show forms on the surface of garnets within 3 min of exposure to ambient moisture and CO_2 , increases the interface (surface) resistance of LLZTO. The plasma treatment is carried out entirely in ambient and is enabled by use of a custom-built metal shroud that is placed around the plasma nozzle to prevent moisture and CO_2 from reacting with the sample. After the plasma treatment, N_2 compressed gas is flowed through the shroud to cool the sample and prevent atmospheric species from reacting with the LLZTO. We demonstrate that this approach is effective for removing the Li_2CO_3 from the surface of LLZTO. The surface chemistry is characterized with X-ray photoelectron spectroscopy to evaluate the effect of process parameters (plasma exposure time and shroud gas chemistry) on removal of the surface species. We also show that the open-air plasma treatment can significantly reduce the interface resistance. This platform demonstrates a path towards open-air processed solid-state batteries.



Citation: Sahal, M.; Guo, J.; Chan, C.K.; Rolston, N. Surface Reduction of Li_2CO_3 on LLZTO Solid-State Electrolyte via Scalable Open-Air Plasma Treatment. *Batteries* **2024**, *10*, 249. <https://doi.org/10.3390/batteries10070249>

Academic Editor: Carolina Rosero-Navarro

Received: 31 May 2024

Revised: 28 June 2024

Accepted: 7 July 2024

Published: 12 July 2024



Copyright: © 2024 by the authors. Licensee MDPI, Basel, Switzerland. This article is an open access article distributed under the terms and conditions of the Creative Commons Attribution (CC BY) license (<https://creativecommons.org/licenses/by/4.0/>).

1. Introduction

Successful synthesis of cubic lithium lanthanum zirconium oxide (c-LLZO) by Murugan et al. in 2007 marked an important milestone in the advancement of garnet-based solid-state electrolytes (SSEs) [1]. Most notably, c-LLZO stands out due to its unique combination of properties, including high Li-ion conductivity at room temperature ($\sim 1 \text{ mS cm}^{-1}$), low activation energy (0.3 eV), excellent oxidation stability at high voltages, and chemical stability against several electrode materials, which is rare among discovered SSEs [2–5]. Ta-doping to form LLZTO has been used more recently to provide the critical Li vacancy concentration needed to stabilize c-LLZO [6,7].

Integrating LLZO into solid-state batteries (SSBs) to match the electrochemical performance of traditional Li-ion batteries using liquid electrolytes presents numerous challenges [8,9]. One significant obstacle is the spontaneous formation of Li_2CO_3 on the surface of LLZO upon exposure to moisture and CO_2 [10,11]. The mechanism of this reaction is well documented [12–15]. This process removes Li from the bulk LLZO structure, resulting in a Li-deficient LLZO phase beneath a newly formed Li_2CO_3 layer [16], which could lead to decreased ionic conductivity. Surface Li_2CO_3 also causes poor contacts at the Li/LLZO interface, resulting in decreased Li-ion transport and higher interface impedance [17,18]. Moreover, Li_2CO_3 accumulated in the LLZO grain boundaries tends to reduce to electronically conductive LiC_x during electrochemical cycling, accelerating the transition of Li ions into Li dendrites [19]. Additionally, phase inhomogeneity caused by Li_2CO_3 at the

electrode–electrolyte interface may result in inferior mechanical properties of the materials and interfaces [20,21].

The effect of Li_2CO_3 on compromising the mechanical, electrochemical, and safety performance of SSBs has been extensively examined in previous work [15,22–26]. Therefore, removing surface Li_2CO_3 from LLZO SSEs emerges as a crucial approach to ensuring optimal electro/chemo/mechanical and safety performance of SSBs. The current methods for removing Li_2CO_3 include mechanical polishing, use of inorganic additives, and thermal treatments under Ar atmosphere, which are time-consuming and difficult to scale up [27–33]. In contrast to this, previous research has demonstrated that scalable, faster processing steps, such as exposure to atmospheric pressure (open-air) plasma, can be effective for contamination removal, activation, and deposition on metal, ceramic, and polymeric surfaces [34–37]. In this work, we investigate the use of an atmospheric pressure (open-air) plasma to remove surface Li_2CO_3 formed on LLZO pellets.

Open-air plasma technology offers a unique opportunity for surface treatments and functionalization by driving reactions and changes to surfaces that are not possible with other plasma or modification approaches [38,39]. The uniqueness of the open-air plasma system is the combination of energy sources which are generated: electrons and reactive species (radicals, metastables, and photons) are produced in combination with convective heat to rapidly transfer energy to enable ultrafast precursor conversion or post-treatment. The blown-arc discharge, open-air plasma configuration used in this work has three key unique features: (1) Potential-free discharge: The plasma discharge is virtually electrically neutral, and the substrate remains free from the electric field of the discharge zone based on a nozzle design that limits the arc discharge [40–42]. This allows for treatment of metals along with electrically sensitive materials, semiconductors, and non-conductive materials. (2) Tunable gas temperature: The electron temperatures in open-air plasmas are usually very high, reaching values $>10,000\text{ }^\circ\text{C}$ [38]. As a result, chemical reactions that take place at high temperatures can be reached (driven by electrons) with significantly reduced heat at values ranging from near-room temperature to $\sim 1500\text{ }^\circ\text{C}$ (Figure S1). The open-air plasma system in this work offers an advantage over conventionally used RF or microwave plasmas because of the opportunity to rapidly transform materials at such a wide and controllable temperature range. (3) Configurability to tune energy fluxes and reactive species: Previous work has shown that changing the nozzle head design can be used to tune the energy flux onto a treated surface [43]. For example, the combination of convective heat along with reactive species has been shown to accelerate the curing of halide perovskite materials above that which can be achieved for the same amount of treatment with compressed gas heated to the same temperature of the plasma [41].

This work includes the addition of an external shroud that was designed to enable injection of externally supplied compressed gas into the region surrounding the plasma. This would allow for displacement of the ambient air molecules and enable the use of a shroud gas after the plasma treatment for cooling of the samples back to room temperature. A schematic representation of the key components of the open-air plasma system, including the custom external shroud, is provided in Figure 1.

The use of N_2 shroud gas for cooling samples following open-air plasma treatment, facilitated by the external shroud, could play a pivotal role in preventing specific reactions that may lead to the reformation of surface Li_2CO_3 on the LLZTO surface. One such reaction is the increased likelihood of CO_2 adsorption, especially at temperatures exceeding $450\text{ }^\circ\text{C}$ [44]. While the adsorption of O_2 on the LLZTO surface is less probable at lower temperatures, higher temperatures create a high-energy surface that may accelerate Li_2CO_3 reformation via Li_2O intermediate [45]. Furthermore, temperatures above $600\text{ }^\circ\text{C}$ may increase the mobility of Li ions, allowing them to penetrate and cross the existing Li_2CO_3 shell on the LLZTO surface, thus promoting the formation of additional Li_2CO_3 layers [46,47]. Thus, by using an external shroud that directs N_2 following open-air plasma treatment, the surface temperature of LLZTO can be kept below $400\text{ }^\circ\text{C}$, which may effectively prevent the conditions for the formation of additional Li_2CO_3 via the aforementioned routes.

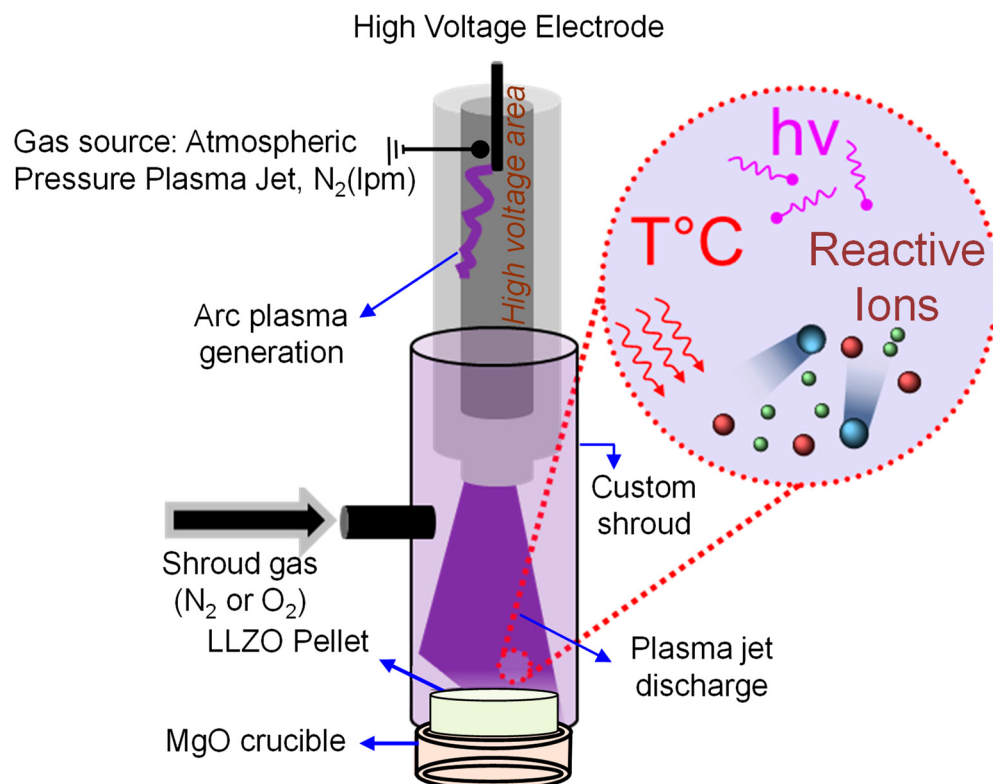


Figure 1. Schematic of custom-built shroud enclosing the open-air plasma nozzle with shroud gas injection for cooling after plasma treatment while maintaining a locally inert environment.

In this work, we demonstrate that the combination of open-air plasma exposure and cooling via shroud gas can be tuned effectively to remove Li_2CO_3 from the surface of LLZTO pellets in an ambient environment. This removal is quantified through surface chemistry characterization and validated with impedance spectroscopy measurements.

2. Materials and Methods

2.1. LLZTO Pellet Preparation

Ta-doped pyrochlores were synthesized through a non-aqueous sol-gel process, detailed in our earlier research, to serve as precursors for LLZTO in a method called pyrochlore-to-garnet (P2G) [48,49]. The nominal composition of the LLZTO is $\text{Li}_{6.4}\text{La}_3\text{Zr}_{1.4}\text{Ta}_{0.6}\text{O}_{12}$. Initially, metal-organic precursors dissolved in propionic acid were combusted at $850\text{ }^\circ\text{C}$ for two hours, forming pyrochlore. Subsequently, this material was ball-milled with LiOH, incorporating a 25 mol% excess of Li, and then formed into pellets under a uniaxial pressure of approximately 300 MPa using a manual hydraulic press, Atlas 15T, (SpecAc, Swedesboro, NJ, USA). Finally, these pellets were sintered at $1100\text{ }^\circ\text{C}$ for 2 h in MgO crucibles within a Li_2O -rich atmosphere in a tube furnace (Lindberg/BlueM TF55030A, Thermo Scientific, New Columbia, PA, USA) with Al_2O_3 tubes and a heating rate of $5\text{ }^\circ\text{C}/\text{min}$. The sintering process is described in detail in our previous work [48,50].

The relative density of the pellets post-sintering were determined through measurements of weight, thickness, and cross-sectional area, then compared to a theoretical density of 5.4 g/cm^3 [51]. Crystal structure analysis was performed using a powder diffractometer (Malvern PANalytical Aeris Research Edition, Worcestershire, UK) with a $\text{CuK}\alpha$ source. The formation of the LLZTO cubic phase was verified by comparing the powder X-ray diffraction (XRD) pattern of the pellets with the LLZTO reference pattern from PDF card 04-018-9024 [52]. The pellets in this study typically featured a cross-section area of approximately 35 mm^2 and a thickness range of $0.5\text{--}0.7\text{ mm}$.

2.2. Open-Air Plasma Conditions

Open-air plasma treatment on LLZTO pellets to remove surface Li_2CO_3 was carried out using a FG5001S - V1.10 Open-air[®] Plasma Generator (Plasmatreat GmbH, Steinhagen, Germany). This system has been shown to be compatible with a range of materials and device structures in previous work [41]. The LLZTO pellets were placed on MgO crucibles serving as substrates during the plasma treatment. The varied plasma conditions in this study included exposure time and the shroud gas environment post-plasma exposure (N_2 or O_2). Figure S2 outlines the steps for preheating and exposing the LLZO pellet to an open-air plasma jet. All treatments had 100% plasma cycle time (duty cycle). The plasma output power, generator DC voltage, and high-voltage transformer current are not directly controlled and remained between 630–645 W, 270–280 V, and 11–12 A, respectively. The N_2 ionization gas flow rate was also kept constant at 20 L per minute (lpm), and the distance between the plasma nozzle and the LLZTO pellet was set at 1 mm. Shroud gas (N_2 or O_2) flow was used for post-plasma treatment cooling with the flow rate kept at 43 lpm for 5 min.

2.3. Materials Characterization

X-ray photoelectron spectroscopy (XPS) was used to analyze the elemental composition and surface chemistry of the LLZTO samples using Axis Supra+ spectrometer (Kratos Analytical Ltd, Manchester, UK). This equipment is equipped with a monochromatic $\text{Al K}\alpha$ X-ray source. The surface morphology of LLZO pellets before and after plasma treatment was characterized using a VHX-7000 Series Digital Microscope (Keyence Corporation of America, Itasca, IL, USA). The as-sintered pellets were manually polished in ambient conditions with a series of SiC sandpapers (240 to 2000 grit, McMaster-Carr) to achieve flat surfaces. Then, the pellets were left out in ambient conditions (RH ~38–43%) for 2 days to form a uniform Li_2CO_3 layer, and thereafter subjected to plasma treatment. Following plasma treatment, the samples were quickly transferred to a glovebox filled with an N_2 atmosphere within 30 s to 1 min. Inside the N_2 glove box, the plasma-treated samples were mounted onto a transfer sample holder provided by Kratos, which can maintain a vacuum created by a mechanical pump. This setup ensured that during transport of the sample holder to the XPS main chamber, the plasma-treated samples remained sealed from the external environment, allowing for an effective evaluation of the impact of open-air plasma treatment on surface Li_2CO_3 reduction. Consequently, the exposure of the LLZTO surface to ambient conditions after open-air plasma treatment was limited to around 30 s to 1 min prior to XPS analysis. For comparison, some LLZTO samples were subjected to Ar^+ sputtering inside the XPS with 20 keV 500 Ar^+ ion clusters (equivalent to 40 eV Ar^+ ions, a process designed not to reduce the elements in the sample [48]). All measured XPS binding energies were calibrated to the C 1s hydrocarbon (C-C) peak at 285 eV [53,54].

The high-resolution Li 1s, O 1s, and C 1s spectral peak components were fitted with CasaXPS software (Version 2.3.25PR1.0) [55]. Backgrounds for these components were quantified using a Shirley-type subtraction method that adjusts to changes in the spectral data, ensuring accurate background computation [56,57]. Additionally, Kratos sensitivity factors specific to the XPS instrument used in this study were applied to enhance the fitting accuracy [57].

To fit peak components in the high-resolution Li, O, and C 1s spectra, we used the Gaussian–Lorentzian sum function $GL(x)$, which represents symmetric XPS signals [58]. In general, the full width at half maximum (FWHM) of these high-resolution Li 1s, O 1s, and C 1s spectral peak components was restricted to values less than 2 eV, as specified in the literature [59,60]. The FWHM for the C=O (Li_2CO_3) and C-C components in the C 1s spectra was limited to 1.1–1.3 eV [61,62]. Meanwhile, for the C-O-C components, the FWHM was allowed to vary between 1.0 and 1.5 eV [62]. For the O 1s spectra, the FWHM for the Li_2CO_3 and metal oxide(s) components was set to 1.4–1.7 eV [59,61,62]. Similarly, the FWHMs of the Li_2CO_3 and Li-O components were allowed to vary between 1.0 and 1.5 eV for the Li 1s spectra [60,63]. In this study, the mixing parameter, α , was 0.7. Thus, the line shape $GL(x)$

became $GL(30) = [0.3 \times L(x)] + [0.7 \times L(x)]$ for XPS signals [61]. The previous literature provides detailed equations for the Gaussian and Lorentzian components, as well as for the FWHM, half width at half maximum (HWHM), and other related parameters [58].

2.4. Electrochemical Impedance Spectroscopy (EIS) Measurements

EIS measurements were conducted at room temperature using a potentiostat (SP-200, BioLogic Science Instruments, Knoxville, TN, USA), spanning a frequency range from 7 MHz to 1 Hz with a 50 mV stimulus voltage. These measurements assessed the interfacial resistance of LLZTO pellets under two distinct conditions: (i) after exposure to ambient atmosphere for 2 days, and (ii) after open-air plasma treatment.

For the latter condition, following plasma treatment, LLZTO pellets were exposed to either O₂ or N₂ shroud gas for 5 min at 43 lpm to cool the sample surface below 200 °C. LLZTO pellets for both conditions were then promptly transferred to an Ar-filled glovebox with minimal exposure to ambient air (approximately 30 s to 1 min). Inside the Ar glovebox, the pellets were vacuum-sealed in heat-sealable polybags. After vacuum sealing, these pellets were moved to another Ar glovebox, where low impedance electrical contacts made of a nonblocking Li/Sn alloy (comprising 20 wt.% or approximately 1.5 mol% Sn) were applied to both sides of each LLZO pellet, creating a layer approximately 100 μm thick, following procedures outlined in previous studies [48,50]. After application of the Li/Sn electrical contacts, copper (Cu) wires were connected to them and the pellet was enclosed in a heat sealable polybag, such that only the Cu wires were extending out. These extended Cu wires were connected to the potentiostat for EIS measurements as described in our prior work [64,65]. The impedance data were fitted as described in our previous work [66].

3. Results and Discussion

3.1. Li₂CO₃ Formation Kinetics

The spontaneous formation of Li₂CO₃ on the surface of garnets has been reported extensively. Following mechanical polishing under inert atmosphere, Sharafi et al. observed the reappearance of the C=O peak associated with Li₂CO₃ on the surface of LLZTO after 7 min of air exposure [67]. However, it is not clear if the Li₂CO₃ levels were measured before polishing, or if the same sample was used to characterize the C 1s spectrum after polishing and air exposure [67]. Apart from this report, there is a limited body of literature exploring the rapidity with which Li₂CO₃ reforms on the LLZTO surface following ambient air exposure. Most studies investigating the detrimental effects of Li₂CO₃ on LLZTO ionic conductivity have utilized longer exposure times, ranging from 15 min to as long as 90 days, as indicated in Table S1. Therefore, the formation kinetics of Li₂CO₃ on LLZTO discussed here hopefully provide some new understanding to the community.

Figure 2a–c shows the high-resolution XPS C 1s spectra obtained on the same LLZTO pellet at three different conditions. Figure 2a shows the spectrum taken following a two-day exposure of the LLZTO surface to ambient air, which results in the formation of surface Li₂CO₃. This pellet was then transferred to the XPS as described in Section 2.3 and subjected to in situ Ar⁺ sputtering to remove the surface Li₂CO₃. The resulting C 1s spectrum is shown in Figure 2b. After the Ar⁺ sputtering, the pellet was re-exposed to ambient conditions for 3 min, and then measured again with XPS at the identical location, resulting in the spectrum shown in Figure 2c.

Table S2 provides the overall atomic concentrations of Li, C, O, La, Ta, and Zr measured on the LLZTO pellets surfaces for all three instances shown in Figure 2a–c, while Figure S3 shows the atomic concentration analysis from the C 1s peak fitting to C=O associated with Li₂CO₃, C-C, and C-O-C for the same cases. Additionally, the corresponding high-resolution O 1s and Li 1s spectra are shown in Figures S4a–c and S5a–c, respectively. The C 1s peaks observed at 290.12 eV in Figure 2a and 289.94 eV in Figure 2c correspond to the C=O peak at ~290 eV, widely reported for Li₂CO₃ present on the surface of LLZO-based SSEs in the literature [11,31,67,68]. There is a slight shift in the C=O peak in Figure 2b to 289.77 eV, which is unexpected and could be due to the uncertainty in aligning the

binding energies to the significantly reduced C-C feature after sputtering. However, this slight shift in binding energy is still within the binding energy values reported for the C=O peak originating from Li_2CO_3 reported elsewhere [68,69]. The C 1s atomic concentration associated with Li_2CO_3 (C=O) intensity diminishes from 16.3% to 2.1% after Ar^+ sputtering but increases to 11.3% when the LLZTO sample surface is re-exposed to ambient air for a three-minute period, as indicated by respective C 1s atomic concentrations shown in Figure S3.

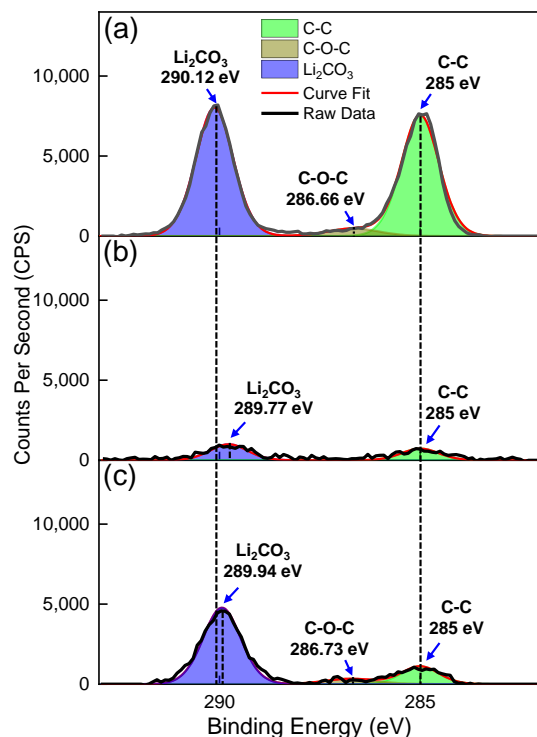


Figure 2. High-resolution XPS C 1s spectra of LLZTO pellet sample at three distinct instances: (a) initially following a two-day exposure of the LLZTO surface to ambient air, resulting in the formation of surface Li_2CO_3 ; (b) immediately after in situ Ar^+ sputtering in the XPS vacuum chamber was performed on the LLZTO surface to remove Li_2CO_3 ; and (c) after three minutes of exposure to ambient following Li_2CO_3 removal by Ar^+ sputtering.

The O 1s spectra shown in Figure S4a–c exhibit a clear correlation with the corresponding C 1s spectra in Figure 2a–c. As illustrated in Figure S4a, following a two-day exposure to ambient air, the O 1s spectrum of the LLZTO surface is primarily a peak at 531.95 eV attributed to Li_2CO_3 , with no clear indication of signals associated with the metal oxide bonding in the lattice of the underlying LLZTO. In contrast, the O 1s spectrum of the LLZTO surface immediately after Ar^+ sputtering, as shown in Figure S4b, indicates the presence of both Li_2CO_3 and metal–oxide bonding in LLZTO. These O 1s peaks at binding energies associated with Li_2CO_3 and the LLZTO lattice are consistent with those reported in the literature for LLZO [28,32,49,70].

After Ar^+ sputtering, the binding energy for the O 1s peak at 531.95 eV associated with Li_2CO_3 on the LLZTO surface shifts to 531.33 eV as the thickness of the Li_2CO_3 layer is reduced. This decrease in the binding energy of the O 1s peak for Li_2CO_3 could be attributed to the interaction of the remaining Li_2CO_3 layer with the underlying LLZTO phase, which may consist of surface states or defects capable of donating electrons and reducing the existing Li_2CO_3 layer.

The O 1s peak observed on the LLZTO surface after a 3 min ambient exposure, as shown in Figure S4c, is at 531.81 eV, which is very close to the O 1s peak binding energy observed on LLZTO after two days of exposure to ambient air. The signal from the LLZTO

lattice is also observed in this case. The largest difference in binding energy between the O 1s peaks associated with Li_2CO_3 and metal–oxide is around 2.3–2.4 eV, as illustrated in Figure S4b,c, which is comparable to the O 1s binding energy difference for Li_2CO_3 and metal–oxide peak positions that have been previously reported [28,49].

Figure S5a–c presents the high-resolution Li 1s spectra corresponding to the cases described in Figure 2a–c. As illustrated in Figure S5a,c, the Li 1s peaks at 55.35 eV and 55.24 eV can be attributed to Li_2CO_3 [71]. Conversely, the Li 1s peak at 54.77 eV observed after Ar^+ sputtering is attributable to Li–O in LLZTO [17]. Furthermore, Figure S5b,c reveal peaks at around 52.70 and 52.24 eV, respectively, which can be attributed to Zr 4s. Figure S6a–c show the corresponding wide scans for each of the cases in Figure 2a–c. Figure S6b,c clearly show the presence of La, Zr, and Ta, which are associated with the LLZTO phase. These data confirm that the Ar^+ sputtering can remove the Li_2CO_3 surface species and reveal the underlying LLZTO, but that Li_2CO_3 can reform and partially cover the LLZTO surface again upon exposure to ambient air after only three minutes.

3.2. Effect of Open-Air Plasma Treatment on Reduction of Surface Li_2CO_3 on LLZTO

The open-air plasma can drive surface chemical reactions through the control of the combination of heat and reactive species from the plasma processing parameters. Specifically, we focus on two parameters: treatment time (5, 10, 20, or 40 min) and shroud gas chemistry (N_2 or O_2) used after treatment.

The effect of open-air plasma treatment was carried out on LLZTO pellets that were initially exposed to ambient air for 2 days prior to the treatment. Each pellet was subjected to different plasma treatment times and the XPS measurement was carried out on the same pellet before and after the treatment, although different pellets were used for each treatment time. Figure 3a–d show the C 1s spectra before and after plasma treatment durations of (a) 5, (b) 10, (c) 20, and (d) 40 min with N_2 ionization gas. The N_2 shroud gas was turned on and flowed for 5 min after each plasma treatment. Figure 3a–d present the normalized peak intensities, which were computed by dividing the values by the greatest intensity measured in counts per second, of each pellet before the plasma treatment.

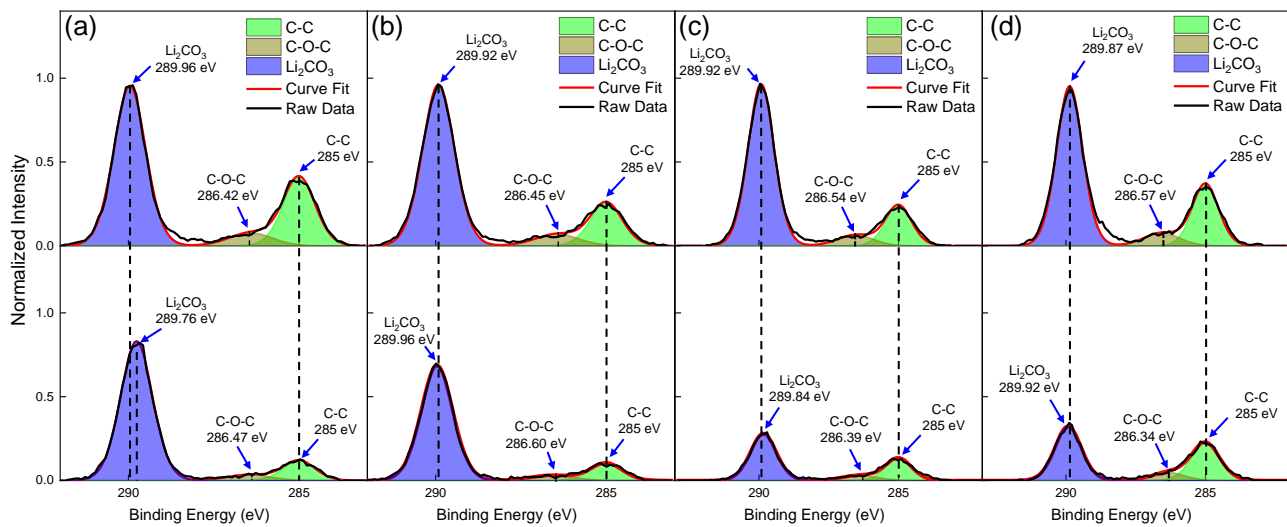


Figure 3. C 1s spectra of the LLZTO surface captured before (on top) and after (on bottom) exposure to open-air plasma for varying durations: (a) 5 min, (b) 10 min, (c) 20 min, and (d) 40 min. Each treatment time was performed on a different pellet.

The XPS results showed that all treatment times studied were effective in reducing surface Li_2CO_3 from LLZTO, but the most significant reduction occurred after exposure to open-air plasma for 20 and 40 min, as indicated in Figure 3c,d, showing a decreased intensity C=O peak intensity associated with Li_2CO_3 for both treatments. Figure S7 presents the C 1s peak fitting results before and after the open-air plasma treatment, revealing a 31% decrease

in Li_2CO_3 ($\text{C}=\text{O}$) peak intensity after 20 min. Estimation of C 1s atomic concentration associated with Li_2CO_3 after 40 min was not very accurate due to the observation of Mg contamination in the sample. This contamination is visible in Figure S8, which shows a higher intensity of Mg KLL, 2s, and 2p characteristic spectral lines following the 40 min treatment in the XPS wide scan. The source of Mg contamination is most likely from the MgO substrate used to support the LLZTO pellet during the plasma treatment.

Interestingly, while the reduction in Li_2CO_3 levels observed for the sample exposed to open-air plasma for 20 min exceeds that of samples exposed for 5 and 10 min, shorter exposure times result in a greater reduction of adventitious carbon (C-C), evident by comparing the peak intensity at 285 eV in Figure 3a,b. Figure S7 shows that the decrease in atomic concentration associated with adventitious carbon (C-C) after 5 and 10 min of open-air plasma exposure is 70% and 52%, respectively. Similarly, Figure S7 shows that shorter durations of open-air plasma exposure (5 and 10 min) result in a greater reduction of C 1s atomic concentration associated with C-O-C than longer durations of open-air plasma exposure (20 min), in accordance with the observed trend for C-C reductions. Thus, there is a clear indication that longer exposure durations, beginning at 5 min, lead to an increase in the magnitude of Li_2CO_3 reduction, whereas the magnitude of C-C and C-O-C reduction decreases over the same durations. Finally, in terms of Li_2CO_3 levels, comparing the results in Figure S7c with those in Figure S3c indicates that LLZTO surfaces after 20 min of open-air plasma exposure are similar to those seen after a 3 min exposure to ambient conditions following Ar^+ sputtering.

3.3. Influence of Shroud Gas on Surface Reduction of Li_2CO_3 on LLZTO

Figure S9a–d show the normalized C 1s spectra from LLZTO surfaces through four panels, before and after plasma treatment with post-treatment using O_2 or N_2 as shroud gas. Both of these cases underwent 10 min open-air plasma treatments with an ionization gas (N_2) flow rate of 20 lpm prior to cooling. The results in Figure S9a–b show that using O_2 as the shroud gas results in a minimal shift in the Li_2CO_3 peak from 290 eV to 289.95 eV. However, Figure S9c,d shows that using N_2 as the shroud gas causes no shift in the Li_2CO_3 peak, indicating that there may be no further chemical reduction of Li_2CO_3 induced by the N_2 shroud gas. Peak fitting results shown in Figure S10 indicate that using O_2 and N_2 as shroud gases reduces the C 1s atomic concentration associated with Li_2CO_3 ($\text{C}=\text{O}$) by 13% and 15%, and C 1s atomic concentration associated with C-C by 63% and 52%, respectively. Thus, the choice of O_2 or N_2 shroud gas for cooling may not significantly affect the efficacy of removing surface contaminants like adventitious carbon (C-C) and Li_2CO_3 .

3.4. Effect of Open-Air Plasma Treatment on LLZTO Crystal Structure and Surface Morphology

Figure S11a shows a comparison of powder XRD patterns obtained for an LLZTO pellet manually polished with sandpaper and subjected to minimal air exposure, after the polished pellet was exposed to air for 2 days, and then after the pellet was subjected to open-air plasma treatment for 20 min, followed by cooling with N_2 shroud gas. All three XRD patterns showed reflections matching the LLZTO reference. The XRD pattern for the pellet after 2 days air exposure had a small peak at $2\theta \sim 21.5^\circ$, which corresponds to the (110) reflections of Li_2CO_3 but was otherwise unchanged from the XRD pattern of the freshly polished sample. After the plasma treatment, the XRD results show that the LLZTO structure remained intact, with no indication of phases that form because of Li-loss, such as pyrochlore ($\text{La}_2\text{Zr}_2\text{O}_7$). However, close inspection of the XRD pattern for the plasma-treated sample shows the presence of several impurity phases such as Li_2O , MgO , ZrO_2 , $\text{Mg}_4\text{Ta}_2\text{O}_9$, and Li_7TaO_6 , as shown in Figure S11b. The minor amount of MgO is consistent with the minor Mg signal observed in the XPS measurements (Figure S8), and is attributed to contamination from the MgO crucible. The presence of Li_2O , ZrO_2 , and Li_7TaO_6 indicates that some of the LLZTO may have decomposed during the plasma treatment, but the presence of $\text{Mg}_4\text{Ta}_2\text{O}_9$ suggests that the Mg contamination may have also contributed to the decomposition reaction(s). Future studies using alternative substrates

to support the LLZTO pellets may better elucidate the role of Mg in the decomposition of LLZTO during the plasma treatment. Nonetheless, the results shown in Figure S11 are good support for the effectiveness of the open-air plasma treatment for reducing the Li_2CO_3 surface content without causing deleterious effects for the LLZTO structure.

Figure S12a–d show the surface morphology of an LLZO pellet before and after 20 min of open-air plasma exposure, followed by a 5 min cooling phase with shroud gas (N_2). Figure S12a,c show laser images of the LLZO pellet surface before and after plasma treatment, respectively. The laser image after the treatment shows a significantly smoother surface topography, as evidenced by a 36% reduction in overall surface height (S_a), as shown in Table S3. However, the optical images in Figure S12b,d, taken before and after plasma treatment, respectively, do not show any significant differences. The decrease in surface roughness parameter is consistent with the etching of the surface layer from the LLZTO pellets during the open-air plasma treatment.

3.5. Effect of Open-Air Plasma Treatment on Interface Resistance and Ionic Conductivity

To examine the impacts of the open-air plasma treatment on the LLZTO interface resistance, we prepared symmetric cells comprising LLZTO pellets in contact with nonblocking electrodes made from Li/Sn alloy. Two pellets were exposed to ambient atmosphere for two days and the XPS spectra (Figure S13) confirmed they had similar levels of surface Li_2CO_3 . Then, a 20 min plasma treatment was performed on one of the pellets (one face only). Figure 4 shows the Nyquist plot obtained for the plasma-treated pellet had a much lower impedance than the one without plasma treatment. The EIS data for the plasma-treated pellet could be fitted with an equivalent circuit of $Q_{\text{tot}}/R_{\text{tot}} + Q_i/R_i$, where R_{tot} is the total (bulk and grain boundary) resistance, R_i is the interface resistance, and Q_{tot} and Q_i are constant phase elements to account for nonideal capacitance (see Table S4 for fitting parameters). From this fitting, the total ionic conductivity of the plasma-treated LLZTO was determined to be 0.14 mS/cm and the interface resistance was ~37 kOhm (12.5 kOhm·cm²). This ionic conductivity value is consistent with our previous observations for pellets with similar relative density of ~78% [49]. Without the plasma treatment, the EIS data could not be fitted to the same equivalent circuit because the interface impedance dominated the Nyquist plot. Using Q_i/R_i for the equivalent circuit, the resistance was determined to be ~68 kOhm (22.4 kOhm·cm²), or almost double the interfacial resistance seen in the sample that was subjected to open-air plasma treatment. The overall interface resistance of the treated pellet is still fairly high, but it is important to note that only one side of the LLZTO pellet was exposed to the plasma. As such, it is likely that Li_2CO_3 on the bottom interface of the pellet greatly increased the interfacial resistance of the measurement. This is a further reason supporting the efficacy of such an approach for LLZTO thin films (i.e., such as those that might be used in anode-free SSBs), where the bottom interface will be bonded to a current collector and protected from atmospheric species.

The observed reduction in interfacial resistance achieved through open-air plasma treatment (approximately 44%) is compared to other reported treatments in Table S5. The reduction is less than that achieved by heating LLZO at 250 °C for 1 h under an inert atmosphere (approximately 70%), a method used to reintegrate Li components from Li_2CO_3 back into LLZO [10,72]. Qualitatively, the heating method significantly reduces the amount of Li_2CO_3 on the LLZTO surfaces, although the degree of reduction was not quantified in the literature for this method. When compared to this method, the open-air plasma treatment has advantages such as not requiring an inert environment and requiring less time to achieve reductions in Li_2CO_3 surface species.

Another high-temperature thermal cleaning method involves heating at elevated temperatures for several hours in an Ar environment. For example, using 900 °C for 1 h leads to a reported reduction in interfacial resistance exceeding 99% [32]. Another study showed that a 2 h treatment of LLZTO at 800 °C in an inert Ar glovebox could greatly help the integration of the SSE into fully operating solid-state Li/S batteries with high sulfur cathode loading [73]. However, this method is not scalable for removing

Li_2CO_3 from LLZTO because it requires high temperatures, long treatment times, and an inert environment.

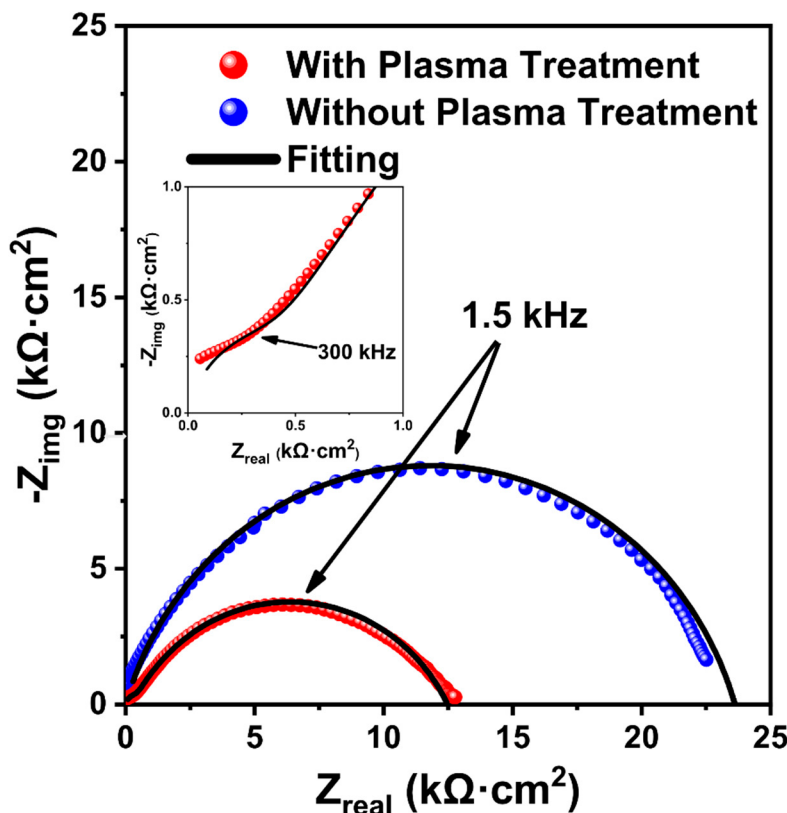


Figure 4. Nyquist plot of the LLZTO pellet measured in a pouch cell observed after 2 days of ambient air exposure and after open-air plasma treatment for 20 min.

Contrary to conventional thermal cleaning methods, a very promising rapid (~2 s) thermal pulse treatment reported recently is also mentioned for Li_2CO_3 reduction. However, its effect on Li_2CO_3 reduction is not as significant as that we observed with the open-air plasma treatment, as evident from the comparison of the C 1s spectra before and after treatment for both methods [74].

In a separate work, applying 2% LiF inorganic additive to the LLZTO provides a slightly lower improvement in interfacial resistance [33]. The advantage of open-air plasma over this method lies in its avoidance of additional complexity in manufacturing and quality control caused by LiF addition. Introducing LiF may demand higher mixing time, and tighter control of LiF particle size and distribution to form a LiF protective layer that can achieve a similar improvement comparable to Li_2CO_3 removal by open-air plasma treatment. Furthermore, as the surface and volume of the electrolyte increase, open-air plasma treatment offers better scalability capabilities through automated systems.

4. Conclusions/Future Work

In this work, we demonstrated the feasibility of using an open-air treatment method to remove Li_2CO_3 and improve the ionic conductivity of LLZTO pellets. In terms of Li_2CO_3 levels, the XPS analysis indicates that LLZTO surfaces after 20 min of open-air plasma exposure are similar to those seen after a 3 min exposure to ambient conditions following Ar^+ sputtering. While open-air plasma treatments may not reduce Li_2CO_3 as effectively as in situ Ar^+ sputtering, they offer considerable benefits. These include a significant decrease in interfacial resistance and the capability to scale up and process larger LLZTO surfaces under normal atmospheric conditions. This makes open-air plasma treatments a potential practical option for removing Li_2CO_3 on LLZTO surfaces.

This advancement is the first such report of enabling open-air processability of LLZTO SSEs. Future work will study the effect of the Li_2CO_3 reformation in plasma-treated LLZTO, as well as the role of the substrate on the formation of secondary phases during the plasma treatment. Additionally, for thin film SSEs on a substrate, the open-air plasma will be better suited for reducing the overall interface resistance since the bottom side will not experience the same Li_2CO_3 growth as was observed in this work for LLZTO pellets.

Supplementary Materials: The following supporting information can be downloaded at: <https://www.mdpi.com/article/10.3390/batteries10070249/s1>, Figure S1. Images of blown arc discharge open-air plasma nozzle; Figure S2. Sequential steps involved in the treatment of LLZO pellets using open air plasma; Figure S3. XPS C1s peak fitting results of the spectra show in Figure 2; Figure S4. XPS O 1s peak fitting results of the spectra shown in Figure 2; Figure S5. XPS Li 1s and Zr 4s peak fitting results of the spectra shown in Figure 2; Figure S6. Wide scan XPS spectra of LLZTO pellet corresponding to cases shown in Figure 2; Figure S7. Reduction in Li_2CO_3 , C-C, and C-O-C surface contaminants after open-air plasma treatment; Figure S8. XPS wide scans after open-air plasma treatment; Figure S9. High-resolution C 1s XPS spectra of LLZTO pellets after 10 minutes of open-air plasma treatment and cooling with different shroud gases; Figure S10. Reduction in Li_2CO_3 , C-C, and C-O-C surface contaminants after 10 minutes of open-air plasma treatment followed by cooling with different shroud gases; Figure S11. Powder XRD patterns of LLZTO pellets after manual polishing, 2 days of air exposure, and 20 minutes of open-air plasma treatment with N_2 cooling, along with relevant reference patterns; Figure S12. Laser and optical images of the LLZTO pellet before and after plasma treatment; Figure S13. High-resolution C 1s XPS spectra of LLZTO pellets exposed for 2 days show comparable Li_2CO_3 levels; one was plasma-treated and the other untreated before Li/Sn electrodes were applied for EIS measurements in Figure 4; Table S1. Previous literature reports on the adverse effects of Li_2CO_3 on LLZO ionic conductivity after exposure to ambient air for different times; Table S2. XPS analysis of LLZTO pellets shows overall atomic concentrations of Li, C, O, La, Ta, and Zr after 2 days of air exposure, in situ Ar^+ sputtering, and 3 minutes of air exposure post-sputtering, with detailed C 1s spectra in Figure 2 and Figure S3; Table S3. Comparison of surface roughness parameter before and after 20-minute open-air plasma treatment; Table S4. EIS fitting parameters in Figure 4 for both untreated and plasma-treated pellets; Table S5. Comparison between the open-air plasma treatment used in this study and existing methods for Li_2CO_3 . References [75–78] are cited in the Supplementary Materials.

Author Contributions: Conceptualization, C.K.C. and N.R.; methodology, M.S. and J.G.; validation, M.S. and J.G.; formal analysis, C.K.C. and N.R.; investigation, M.S. and J.G.; writing—original draft preparation, M.S.; writing—review and editing, J.G., C.K.C. and N.R.; visualization, M.S. and J.G.; supervision, C.K.C. and N.R.; project administration, C.K.C. and N.R.; funding acquisition, C.K.C. and N.R. All authors have read and agreed to the published version of the manuscript.

Funding: This work was supported by the National Science Foundation (NSF) through award TI-2234636.

Data Availability Statement: Data will be made available upon reasonable request.

Acknowledgments: We acknowledge resources and support from the Advanced Electronics and Photonics Core Facility at Arizona State University. We acknowledge the use of facilities within the Eyring Materials Center at Arizona State University supported in part by NNCI-ECCS-1542160. We would also like to acknowledge Daphne Pappas of Plasmatreat USA Inc. and Xin Guo of the Eyring Materials Center for helpful discussions.

Conflicts of Interest: The authors have no conflicts of interest to report.

References

- Murugan, R.; Thangadurai, V.; Weppner, W. Fast Lithium Ion Conduction in Garnet-type $\text{Li}_7\text{La}_3\text{Zr}_2\text{O}_{12}$. *Angew. Chem. Int. Ed.* **2007**, *46*, 7778–7781. [[CrossRef](#)] [[PubMed](#)]
- Samson, A.J.; Hofstetter, K.; Bag, S.; Thangadurai, V. A Bird’s-Eye View of Li-Stuffed Garnet-Type $\text{Li}_7\text{La}_3\text{Zr}_2\text{O}_{12}$ Ceramic Electrolytes for Advanced All-Solid-State Li Batteries. *Energy Environ. Sci.* **2019**, *12*, 2957–2975. [[CrossRef](#)]
- Xu, L.; Li, J.; Deng, W.; Shuai, H.; Li, S.; Xu, Z.; Li, J.; Hou, H.; Peng, H.; Zou, G. Garnet Solid Electrolyte for Advanced All-solid-state Li Batteries. *Adv. Energy Mater.* **2021**, *11*, 2000648. [[CrossRef](#)]

4. Jia, M.; Zhao, N.; Huo, H.; Guo, X. Comprehensive Investigation into Garnet Electrolytes toward Application-Oriented Solid Lithium Batteries. *Electrochem. Energy Rev.* **2020**, *3*, 656–689. [[CrossRef](#)]
5. Abouali, S.; Yim, C.-H.; Merati, A.; Abu-Lebdeh, Y.; Thangadurai, V. Garnet-Based Solid-State Li Batteries: From Materials Design to Battery Architecture. *ACS Energy Lett.* **2021**, *6*, 1920–1941. [[CrossRef](#)]
6. Thompson, T.; Wolfenstine, J.; Allen, J.L.; Johannes, M.; Huq, A.; David, I.N.; Sakamoto, J. Tetragonal vs. Cubic Phase Stability in Al-Free Ta Doped $\text{Li}_7\text{La}_3\text{Zr}_2\text{O}_{12}$ (LLZO). *J. Mater. Chem. A Mater.* **2014**, *2*, 13431–13436. [[CrossRef](#)]
7. Ma, K.; Chen, B.; Li, C.-X.; Thangadurai, V. Improvement of the Li-Ion Conductivity and Air Stability of the Ta-Doped $\text{Li}_7\text{La}_3\text{Zr}_2\text{O}_{12}$ Electrolyte via Ga Co-Doping and Its Application in Li-S Batteries. *J. Mater. Chem. A Mater.* **2024**, *12*, 3601–3615. [[CrossRef](#)]
8. Wu, Z.; Xie, Z.; Yoshida, A.; Wang, Z.; Hao, X.; Abudula, A.; Guan, G. Utmost Limits of Various Solid Electrolytes in All-Solid-State Lithium Batteries: A Critical Review. *Renew. Sustain. Energy Rev.* **2019**, *109*, 367–385. [[CrossRef](#)]
9. Oh, P.; Lee, H.; Park, S.; Cha, H.; Kim, J.; Cho, J. Improvements to the Overpotential of All-solid-state Lithium-ion Batteries during the Past Ten Years. *Adv. Energy Mater.* **2020**, *10*, 2000904. [[CrossRef](#)]
10. Huo, H.; Luo, J.; Thangadurai, V.; Guo, X.; Nan, C.-W.; Sun, X. Li_2CO_3 : A Critical Issue for Developing Solid Garnet Batteries. *ACS Energy Lett.* **2019**, *5*, 252–262. [[CrossRef](#)]
11. Yi, X.; Guo, Y.; Pan, S.; Wang, Y.; Chi, S.; Wu, S.; Yang, Q.-H. Duality of Li_2CO_3 in Solid-State Batteries. *Trans. Tianjin Univ.* **2023**, *29*, 73–87. [[CrossRef](#)]
12. Feng, W.; Zhao, Y.; Xia, Y. Solid Interfaces for the Garnet Electrolytes. *Adv. Mater.* **2024**, *36*, 2306111. [[CrossRef](#)] [[PubMed](#)]
13. Han, S.; Wang, Z.; Ma, Y.; Zhang, Y.; Wang, Y.; Wang, X. Recent Advances in Solving Li_2CO_3 Problems in Garnet-Based Solid-State Battery: A Systematic Review (2020–2023). *J. Energy Chem.* **2024**, *90*, 58–76. [[CrossRef](#)]
14. Familoni, O.; Zhou, Y.; Duan, H. Air Stability of LLZO Electrolytes. In *Solid Electrolytes for Advanced Applications*; Springer: Berlin/Heidelberg, Germany, 2019; pp. 69–89.
15. Wang, J.; Chen, L.; Li, H.; Wu, F. Anode Interfacial Issues in Solid-state Li Batteries: Mechanistic Understanding and Mitigating Strategies. *Energy Environ. Mater.* **2023**, *6*, e12613. [[CrossRef](#)]
16. Hofstetter, K.; Samson, A.J.; Narayanan, S.; Thangadurai, V. Present Understanding of the Stability of Li-Stuffed Garnets with Moisture, Carbon Dioxide, and Metallic Lithium. *J. Power Sources* **2018**, *390*, 297–312. [[CrossRef](#)]
17. Wu, J.-F.; Pu, B.-W.; Wang, D.; Shi, S.-Q.; Zhao, N.; Guo, X.; Guo, X. In Situ Formed Shields Enabling Li_2CO_3 -Free Solid Electrolytes: A New Route to Uncover the Intrinsic Lithiophilicity of Garnet Electrolytes for Dendrite-Free Li-Metal Batteries. *ACS Appl. Mater. Interfaces* **2018**, *11*, 898–905. [[CrossRef](#)] [[PubMed](#)]
18. Cheng, L.; Wu, C.H.; Jarry, A.; Chen, W.; Ye, Y.; Zhu, J.; Kostecki, R.; Persson, K.; Guo, J.; Salmeron, M. Interrelationships among Grain Size, Surface Composition, Air Stability, and Interfacial Resistance of Al-Substituted $\text{Li}_7\text{La}_3\text{Zr}_2\text{O}_{12}$ Solid Electrolytes. *ACS Appl. Mater. Interfaces* **2015**, *7*, 17649–17655. [[CrossRef](#)] [[PubMed](#)]
19. Biao, J.; Han, B.; Cao, Y.; Li, Q.; Zhong, G.; Ma, J.; Chen, L.; Yang, K.; Mi, J.; Deng, Y. Inhibiting Formation and Reduction of Li_2CO_3 to LiCx at Grain Boundaries in Garnet Electrolytes to Prevent Li Penetration. *Adv. Mater.* **2023**, *35*, 2208951. [[CrossRef](#)] [[PubMed](#)]
20. Yan, G. *Mechanical Behavior of Solid Electrolyte Materials for Lithium-Ion Batteries*; RWTH Aachen University: Aachen, Germany, 2020.
21. Wang, S.; Barks, E.; Lin, P.-T.; Xu, X.; Melamed, C.; McConohy, G.; Nemsak, S.; Chueh, W. Effect of H^+ Exchange & Surface Impurities on Bulk & Interfacial Electrochemistry of Garnet Solid Electrolytes. *Mater. Sci.* **2024**. [[CrossRef](#)]
22. Yoon, G.; Kim, S.; Kim, J. Design Strategies for Anodes and Interfaces Toward Practical Solid-State Li-Metal Batteries. *Adv. Sci.* **2023**, *10*, 2302263. [[CrossRef](#)]
23. Ji, W.; Luo, B.; Yu, G.; Wang, Q.; Zhang, Z.; Tian, Y.; Liu, Z.; Ji, W.; Nong, Y.; Wang, X. A Review of Challenges and Issues Concerning Interfaces for Garnet-Type All-Solid-State Batteries. *J. Alloys Compd.* **2024**, *979*, 173530. [[CrossRef](#)]
24. Miao, X.; Guan, S.; Ma, C.; Li, L.; Nan, C. Role of Interfaces in Solid-State Batteries. *Adv. Mater.* **2023**, *35*, 2206402. [[CrossRef](#)]
25. Sun, H.; Celadon, A.; Cloutier, S.G.; Al-Haddad, K.; Sun, S.; Zhang, G. Lithium Dendrites in All-solid-state Batteries: From Formation to Suppression. *Battery Energy* **2024**, *3*, 20230062. [[CrossRef](#)]
26. Kodgire, P.; Tripathi, B.; Chandra, P. Review of Garnet-Based Solid Electrolytes for Li-Ion Batteries (LIBs). *J. Electron. Mater.* **2024**, *53*, 2203–2228. [[CrossRef](#)]
27. Zhang, S.; Zhao, H.; Wang, J.; Xu, T.; Zhang, K.; Du, Z. Enhanced Densification and Ionic Conductivity of Li-Garnet Electrolyte: Efficient Li_2CO_3 Elimination and Fast Grain-Boundary Transport Construction. *Chem. Eng. J.* **2020**, *393*, 124797. [[CrossRef](#)]
28. Li, J.; Gong, Z.; Xie, W.; Yu, S.; Wei, Y.; Li, D.; Yang, L.; Chen, D.; Li, Y.; Chen, Y. Growth Process and Removal of Interface Contaminants for Garnet-Based Solid-State Lithium Metal Batteries. *ACS Appl. Energy Mater.* **2023**, *6*, 12432–12441. [[CrossRef](#)]
29. Liu, J.; Guo, W.; Guo, H.; Xu, C.; Zhang, L.; Chen, Y.; Shen, F.; Han, X. A Simple and Efficient Strategy for Ameliorating Li/LLZO Interfacial Contact. *Energy Fuels* **2022**, *36*, 8500–8505. [[CrossRef](#)]
30. Xu, J.; Tian, W.; Lu, K.; Shan, S.; Zhang, J.; Wu, Y.; Wu, M.; Tang, W. Effect of Acid Treatment of $\text{Li}_7\text{La}_3\text{Zr}_2\text{O}_{12}$ on Ionic Conductivity of Composite Solid Electrolytes. *IOP Conf. Ser. Earth Environ. Sci.* **2020**, *512*, 012110. [[CrossRef](#)]
31. Huo, H.; Chen, Y.; Zhao, N.; Lin, X.; Luo, J.; Yang, X.; Liu, Y.; Guo, X.; Sun, X. In-Situ Formed Li_2CO_3 -Free Garnet/Li Interface by Rapid Acid Treatment for Dendrite-Free Solid-State Batteries. *Nano Energy* **2019**, *61*, 119–125. [[CrossRef](#)]

32. Zhang, H.; Paggiaro, G.; Okur, F.; Huwiler, J.; Cancellieri, C.; Jeurgens, L.P.H.; Chernyshov, D.; van Beek, W.; Kovalenko, M.V.; Kravchyk, K.V. On High-Temperature Thermal Cleaning of $\text{Li}_7\text{La}_3\text{Zr}_2\text{O}_{12}$ Solid-State Electrolytes. *ACS Appl. Energy Mater.* **2023**, *6*, 6972–6980. [[CrossRef](#)]
33. Li, Y.; Xu, B.; Xu, H.; Duan, H.; Lü, X.; Xin, S.; Zhou, W.; Xue, L.; Fu, G.; Manthiram, A. Hybrid Polymer/Garnet Electrolyte with a Small Interfacial Resistance for Lithium-ion Batteries. *Angew. Chem. Int. Ed.* **2017**, *56*, 753–756. [[CrossRef](#)]
34. Noeske, M.; Degenhardt, J.; Strudthoff, S.; Lommatsch, U. Plasma Jet Treatment of Five Polymers at Atmospheric Pressure: Surface Modifications and the Relevance for Adhesion. *Int. J. Adhes. Adhes.* **2004**, *24*, 171–177. [[CrossRef](#)]
35. Kim, M.C.; Yang, S.H.; Boo, J.-H.; Han, J.G. Surface Treatment of Metals Using an Atmospheric Pressure Plasma Jet and Their Surface Characteristics. *Surf. Coat. Technol.* **2003**, *174–175*, 839–844. [[CrossRef](#)]
36. Fridman, A. *Plasma Chemistry*; Cambridge University Press: Cambridge, UK, 2008; ISBN 9781139471732.
37. Lopes, B.B.; Ayres, A.P.A.; Lopes, L.B.; Negreiros, W.M.; Giannini, M. The Effect of Atmospheric Plasma Treatment of Dental Zirconia Ceramics on the Contact Angle of Water. *Appl. Adhes. Sci.* **2014**, *2*, 17. [[CrossRef](#)]
38. Bárdos, L.; Baránková, H. Cold Atmospheric Plasma: Sources, Processes, and Applications. *Thin Solid. Film.* **2010**, *518*, 6705–6713. [[CrossRef](#)]
39. Zabidi, N.Z.A.; Zaaba, S.K.; Sut, K.D.E.; Mohamad, C.; Masiman, R.I. A Brief Review on Atmospheric Air Plasma. In Proceedings of the Journal of Physics: Conference Series; IOP Publishing: Bristol, UK, 2021; Volume 2071, p. 012004.
40. Rolston, N.; Scheideler, W.J.; Flick, A.C.; Chen, J.P.; Elmaraghi, H.; Sleugh, A.; Zhao, O.; Woodhouse, M.; Dauskardt, R.H. Rapid Open-Air Fabrication of Perovskite Solar Modules. *Joule* **2020**, *4*, 2675–2692. [[CrossRef](#)]
41. Rolston, N.; Sleugh, A.; Chen, J.P.; Zhao, O.; Colburn, T.W.; Flick, A.C.; Dauskardt, R.H. Perspectives of Open-Air Processing to Enable Perovskite Solar Cell Manufacturing. *Front. Energy Res.* **2021**, *9*, 684082. [[CrossRef](#)]
42. Hovish, M.Q.; Hilt, F.; Rolston, N.; Xiao, Q.; Dauskardt, R.H. Open Air Plasma Deposition of Superhydrophilic Titania Coatings. *Adv. Funct. Mater.* **2019**, *29*, 1806421. [[CrossRef](#)]
43. Kewitz, T.; Regula, C.; Fröhlich, M.; Ihde, J.; Kersten, H. Influence of the Nozzle Head Geometry on the Energy Flux of an Atmospheric Pressure Plasma Jet. *EPJ Techn Instrum.* **2021**, *8*, 1. [[CrossRef](#)]
44. Xia, W.; Xu, B.; Duan, H.; Tang, X.; Guo, Y.; Kang, H.; Li, H.; Liu, H. Reaction Mechanisms of Lithium Garnet Pellets in Ambient Air: The Effect of Humidity and CO_2 . *J. Am. Ceram. Soc.* **2017**, *100*, 2832–2839. [[CrossRef](#)]
45. Sharifi, A. *Microstructural and Interface Engineering of Garnet-Type Fast Li-Ion-Conductor for Use in Solid-State Batteries*; University of Michigan: Ann Arbor, MI, USA, 2017.
46. Mosqueda, H.A.; Vazquez, C.; Bosch, P.; Pfeiffer, H. Chemical Sorption of Carbon Dioxide (CO_2) on Lithium Oxide (Li_2O). *Chem. Mater.* **2006**, *18*, 2307–2310. [[CrossRef](#)]
47. Pfeiffer, H.; Sánchez-Sánchez, J.; Álvarez, L.J. Lithium and Tritium Diffusion in Lithium Oxide (Li_2O), a Molecular Dynamics Simulation. *J. Nucl. Mater.* **2000**, *280*, 295–303. [[CrossRef](#)]
48. Guo, J.; Weller, J.M.; Yang, S.; Bhat, M.H.; Chan, C.K. Reactive Sintering of Garnet-Type $\text{Li}_{6.4}\text{La}_3\text{Zr}_{1.4}\text{Ta}_{0.6}\text{O}_{12}$ (LLZTO) from Pyrochlore Precursors Prepared Using a Non-Aqueous Sol-Gel Method. *Ionics* **2023**, *29*, 581–590. [[CrossRef](#)]
49. Guo, J.; Chan, C.K. Lithium Dendrite Propagation in Ta-Doped $\text{Li}_7\text{La}_3\text{Zr}_2\text{O}_{12}$ (LLZTO): Comparison of Reactively Sintered Pyrochlore-to-Garnet vs. LLZTO by Solid-State Reaction and Conventional Sintering. *ACS Appl. Mater. Interfaces* **2024**, *16*, 4519–4529. [[CrossRef](#)]
50. Weller, J.M.; Whetten, J.A.; Chan, C.K. Nonaqueous Polymer Combustion Synthesis of Cubic $\text{Li}_7\text{La}_3\text{Zr}_2\text{O}_{12}$ Nanopowders. *ACS Appl. Mater. Interfaces* **2020**, *12*, 953–962. [[CrossRef](#)] [[PubMed](#)]
51. Badami, P.; Weller, J.M.; Wahab, A.; Redhammer, G.; Ladenstein, L.; Rettenwander, D.; Wilkening, M.; Chan, C.K.; Kannan, A.N.M. Highly Conductive Garnet-Type Electrolytes: Access to $\text{Li}_{6.5}\text{La}_3\text{Zr}_{1.5}\text{Ta}_{0.5}\text{O}_{12}$ Prepared by Molten Salt and Solid-State Methods. *ACS Appl. Mater. Interfaces* **2020**, *12*, 48580–48590. [[CrossRef](#)] [[PubMed](#)]
52. Li, Y.; Han, J.-T.; Wang, C.-A.; Xie, H.; Goodenough, J.B. Optimizing Li^+ Conductivity in a Garnet Framework. *J. Mater. Chem.* **2012**, *22*, 15357–15361. [[CrossRef](#)]
53. NIST X-ray Photoelectron Spectroscopy Database. *NIST Standard Reference Database Number 20*; National Institute of Standards and Technology: Gaithersburg, MD, USA, 2000.
54. Greczynski, G.; Hultman, L. Referencing to Adventitious Carbon in X-Ray Photoelectron Spectroscopy: Can Differential Charging Explain C 1s Peak Shifts? *Appl. Surf. Sci.* **2022**, *606*, 154855. [[CrossRef](#)]
55. Fairley, N.; Fernandez, V.; Richard-Plouet, M.; Guillot-Deudon, C.; Walton, J.; Smith, E.; Flahaut, D.; Greiner, M.; Biesinger, M.; Tougaard, S. Systematic and Collaborative Approach to Problem Solving Using X-ray Photoelectron Spectroscopy. *Appl. Surf. Sci. Adv.* **2021**, *5*, 100112. [[CrossRef](#)]
56. Shirley, D.A. High-Resolution X-Ray Photoemission Spectrum of the Valence Bands of Gold. *Phys. Rev. B* **1972**, *5*, 4709. [[CrossRef](#)]
57. Sharifi, A.; Kazyak, E.; Davis, A.L.; Yu, S.; Thompson, T.; Siegel, D.J.; Dasgupta, N.P.; Sakamoto, J. Surface Chemistry Mechanism of Ultra-Low Interfacial Resistance in the Solid-State Electrolyte $\text{Li}_7\text{La}_3\text{Zr}_2\text{O}_{12}$. *Chem. Mater.* **2017**, *29*, 7961–7968. [[CrossRef](#)]
58. Jain, V.; Biesinger, M.C.; Linford, M.R. The Gaussian-Lorentzian Sum, Product, and Convolution (Voigt) Functions in the Context of Peak Fitting X-Ray Photoelectron Spectroscopy (XPS) Narrow Scans. *Appl. Surf. Sci.* **2018**, *447*, 548–553. [[CrossRef](#)]
59. Wood, K.N.; Teeter, G. XPS on Li-Battery-Related Compounds: Analysis of Inorganic SEI Phases and a Methodology for Charge Correction. *ACS Appl. Energy Mater.* **2018**, *1*, 4493–4504. [[CrossRef](#)]

60. Wei, Y.; Xu, H.; Cheng, H.; Guan, W.; Yang, J.; Li, Z.; Huang, Y. An Oxygen Vacancy-Rich ZnO Layer on Garnet Electrolyte Enables Dendrite-Free Solid State Lithium Metal Batteries. *Chem. Eng. J.* **2022**, *433*, 133665. [[CrossRef](#)]
61. Lourens, F.; Rogalla, D.; Suhr, E.; Ludwig, A. On the Influence of Annealing on the Compositional and Crystallographic Properties of Sputtered Li-Al-O Thin Films. *arXiv* **2024**, arXiv:2402.06553.
62. Fantin, R.; Van Roekeghem, A.; Benayad, A. Revisiting Co 2p Core-level Photoemission in LiCoO₂ by In-lab Soft and Hard X-ray Photoelectron Spectroscopy: A Depth-dependent Study of Cobalt Electronic Structure. *Surf. Interface Anal.* **2023**, *55*, 489–495. [[CrossRef](#)]
63. Jones, J.C.; Rajendran, S.; Pilli, A.; Lee, V.; Chugh, N.; Arava, L.M.R.; Kelber, J.A. In Situ X-ray Photoelectron Spectroscopy Study of Lithium Carbonate Removal from Garnet-Type Solid-State Electrolyte Using Ultra High Vacuum Techniques. *J. Vac. Sci. Technol. A* **2020**, *38*, 023201. [[CrossRef](#)]
64. Weller, J.M.; Chan, C.K. Synthesis of Nanostructured Garnets. In *Solid Electrolytes for Advanced Applications*; Springer: Berlin/Heidelberg, Germany, 2019; pp. 25–68.
65. Chan, C.K.; Yang, T.; Weller, J.M. Nanostructured Garnet-Type Li₇La₃Zr₂O₁₂: Synthesis, Properties, and Opportunities as Electrolytes for Li-Ion Batteries. *Electrochim. Acta* **2017**, *253*, 268–280. [[CrossRef](#)]
66. Weller, J.M.; Chan, C.K. Reduction in Formation Temperature of Ta-Doped Lithium Lanthanum Zirconate by Application of Lux–Flood Basic Molten Salt Synthesis. *ACS Appl. Energy Mater.* **2020**, *3*, 6466–6475. [[CrossRef](#)]
67. Sharafi, A.; Yu, S.; Naguib, M.; Lee, M.; Ma, C.; Meyer, H.M.; Nanda, J.; Chi, M.; Siegel, D.J.; Sakamoto, J. Impact of Air Exposure and Surface Chemistry on Li–Li₇La₃Zr₂O₁₂ Interfacial Resistance. *J. Mater. Chem. A Mater.* **2017**, *5*, 13475–13487. [[CrossRef](#)]
68. Zhou, X.; Liu, J.; Ouyang, Z.; Liu, F.; Zhang, Z.; Lai, Y.; Li, J.; Jiang, L. In-Situ Construction of Electronically Insulating and Air-Stable Ionic Conductor Layer on Electrolyte Surface and Grain Boundary to Enable High-Performance Garnet-Type Solid-State Batteries. *Small* **2024**, 2402086. [[CrossRef](#)] [[PubMed](#)]
69. Contarini, S.; Rabalais, J.W. Ion Bombardment-Induced Decomposition of Li and Ba Sulfates and Carbonates Studied by X-Ray Photoelectron Spectroscopy. *J. Electron. Spectros Relat. Phenomena* **1985**, *35*, 191–201. [[CrossRef](#)]
70. Vema, S.; Sayed, F.N.; Nagendran, S.; Karagoz, B.; Sternemann, C.; Paulus, M.; Held, G.; Grey, C.P. Understanding the Surface Regeneration and Reactivity of Garnet Solid-State Electrolytes. *ACS Energy Lett.* **2023**, *8*, 3476–3484. [[CrossRef](#)] [[PubMed](#)]
71. Cheng, L.; Crumlin, E.J.; Chen, W.; Qiao, R.; Hou, H.; Lux, S.F.; Zorba, V.; Russo, R.; Kostecki, R.; Liu, Z. The Origin of High Electrolyte–Electrode Interfacial Resistances in Lithium Cells Containing Garnet Type Solid Electrolytes. *Phys. Chem. Chem. Phys.* **2014**, *16*, 18294–18300. [[CrossRef](#)] [[PubMed](#)]
72. Cheng, L.; Liu, M.; Mehta, A.; Xin, H.; Lin, F.; Persson, K.; Chen, G.; Crumlin, E.J.; Doeff, M. Garnet Electrolyte Surface Degradation and Recovery. *ACS Appl. Energy Mater.* **2018**, *1*, 7244–7252. [[CrossRef](#)]
73. Shi, C.; Takeuchi, S.; Alexander, G.V.; Hamann, T.; O'Neill, J.; Dura, J.A.; Wachsman, E.D. High Sulfur Loading and Capacity Retention in Bilayer Garnet Sulfurized-Polyacrylonitrile/Lithium-Metal Batteries with Gel Polymer Electrolytes. *Adv. Energy Mater.* **2023**, *13*, 2301656. [[CrossRef](#)]
74. Wang, C.; Xie, H.; Ping, W.; Dai, J.; Feng, G.; Yao, Y.; He, S.; Weaver, J.; Wang, H.; Gaskell, K. A General, Highly Efficient, High Temperature Thermal Pulse toward High Performance Solid State Electrolyte. *Energy Storage Mater.* **2019**, *17*, 234–241. [[CrossRef](#)]
75. Xia, W.; Xu, B.; Duan, H.; Guo, Y.; Kang, H.; Li, H.; Liu, H. Ionic Conductivity and Air Stability of Al-Doped Li₇La₃Zr₂O₁₂ Sintered in Alumina and Pt Crucibles. *ACS Appl. Mater. Interfaces* **2016**, *8*, 5335–5342. [[CrossRef](#)]
76. Lu, W.; Wang, T.; Xue, M.; Zhang, C. Improved Li_{6.5}La₃Zr_{1.5}Nb_{0.5}O₁₂ Electrolyte and Effects of Atmosphere Exposure on Conductivities. *J. Power Sources* **2021**, *497*, 229845. [[CrossRef](#)]
77. Lan, W.; Lu, D.; Zhao, R.; Chen, H. Investigation of Al₂O₃ Crucible Contamination Induced by Extra Li₂CO₃ during Li₇La₃Zr₂O₁₂ Solid Electrolyte Sintering Process. *Int. J. Electrochem. Sci.* **2019**, *14*, 9695–9703. [[CrossRef](#)]
78. Brugge, R.H.; Hekselman, A.K.O.; Cavallaro, A.; Pesci, F.M.; Chater, R.J.; Kilner, J.A.; Aguadero, A. Garnet Electrolytes for Solid State Batteries: Visualization of Moisture-Induced Chemical Degradation and Revealing Its Impact on the Li-Ion Dynamics. *Chem. Mater.* **2018**, *30*, 3704–3713. [[CrossRef](#)]

Disclaimer/Publisher’s Note: The statements, opinions and data contained in all publications are solely those of the individual author(s) and contributor(s) and not of MDPI and/or the editor(s). MDPI and/or the editor(s) disclaim responsibility for any injury to people or property resulting from any ideas, methods, instructions or products referred to in the content.